



Optimized optical propagation through underwater turbulence using off-axis Bessel-Gauss beam probing

JAXON P. WILEY,¹ EVAN ROBERTSON,¹ TYLER CRAMER,¹ J. KEITH MILLER,^{1,2}  AND ERIC G. JOHNSON^{2,*}

¹Holcombe Department of Electrical and Computer Engineering, Clemson University, Clemson, SC 29634, USA

²CREOL, The College of Optics and Photonics, University of Central Florida, Orlando, FL 32816, USA
[*eric.johnson2@ucf.edu](mailto:eric.johnson2@ucf.edu)

Abstract: Off-axis Bessel-Gauss (BG) beams are used as a generation basis within an optical system that rapidly probes an underwater turbulent environment. Due to the rapidity of the scan, implemented using a modified Higher Order Bessel Beams Integrated with Time (HOBBIT) system, instantaneous realizations of the turbulence can be probed allowing optimal transmission paths in which the beams propagate, with minimal perturbations, through the complex turbulent environment. The results show a marked reduction in the effects of the turbulence, including over a 91% decrease in scintillation index, experienced by the beams propagated through these paths when compared to a centered on-axis BG beam. Results also confirm the ability to transmit higher-order BG beams. Lastly, the spatial and temporal characteristics of these robust channels are presented, demonstrating the propensity to transmit multiple beams through unperturbed transmission paths simultaneously.

© 2025 Optica Publishing Group under the terms of the [Optica Open Access Publishing Agreement](#)

1. Introduction

Surfacing over 70% of the globe, the world's underwater environments present a relatively unexplored frontier, teeming with potential applications in sensing for understanding the ocean and its complex ecosystem. Recently, there has been an influx of attention devoted to these environments and the technologies used to explore them. In particular, the development of underwater optical systems has shown great promise due to the inherent advantages they offer over more traditional techniques, such as RF or acoustic-based systems [1]. However, when considering optical systems in underwater conditions, turbulence presents a complex obstacle that must be addressed. Underwater optical turbulence, defined as fluctuations in the refractive index of water, is primarily driven by environmental factors such as temperature and salinity. These fluctuations can cause distortion, breakup, and deflection, resulting in significant variations in the intensity of propagated beams and overall system degradation [2–4]. These adverse effects have been reported in numerous publications, including the experimentally measured power-loss due to underwater turbulence [5], the effects of weak turbulence conditions on the scintillation index [6], and the analysis of system performance parameters in simulated underwater turbulence [7,8].

Several techniques have been proposed to mitigate the impact of underwater turbulence, including adaptive optics, spatial diversity, and aperture averaging [9–14]. Additionally, an approach that has gained recent attention is the customization of structured light to boost the performance of optical systems in turbulent environments. Structured light, used extensively in the optical system community, refers to the tailoring of light modes using various degrees of spatial freedom, such as polarization, amplitude, and phase [15]. Two common classes of structured modes include those with Orbital Angular Momentum (OAM), where the phase is

azimuthally wrapped around the propagation path [16–18], and non-diffracting beams, whose intensity profiles propagate without diffraction over significant distances [19]. A common class of these non-diffracting beams is the Bessel-Gauss (BG) beam set, which is the Gaussian apodization of the well-known Bessel beam [20,21]. BG beams have shown tremendous potential in turbulent environments, with studies demonstrating increased resilience and improved data transmission through turbulent paths when compared to Gaussian beams [22,23]. With these encouraging results, it is important to note that these beams are not totally impervious to the effects of turbulence and are still vulnerable to distortion and deflection in underwater turbulence. Thus, merely propagating a beam without considering the environment through which it propagates will consistently limit that beam's performance. To address this issue, recent studies describe the tailoring of light modes to ensure unperturbed transmission in a given basis through a turbulent path [24–26]. These studies demonstrate the ability to generate eigenmodes of a certain turbulent path such that the beams are preserved following propagation through the specific path, representing a crucial advancement in the optimization of optical systems in non-ideal environments. With the mentioned works utilizing phase screens to simulate a turbulent volume, the question then arises on how to achieve similar unperturbed transmission in a dynamic, real-world turbulent environment.

In this work, we leverage inherent advantages of BG beams within an optical setup capable of rapidly probing a volume, demonstrating the ability to identify and exploit unperturbed transmission paths in dynamic underwater turbulence. The rapidity of the scanning system, based on the modified Higher Order Bessel Beams Integrated in Time (HOBBIT) architecture [27], allows instantaneous realizations of the dynamic turbulent environment to be probed. This generation basis shifts, rather than tilts, a BG beam off-axis within a volume of the turbulent environment, identifying transmission channels through the medium where the beam transmits unperturbed. Figure 1(a),(b) depicts a single instance of an (b) off-axis BG beam within the turbulent volume, resulting in relatively unperturbed transmission when compared to the (a)

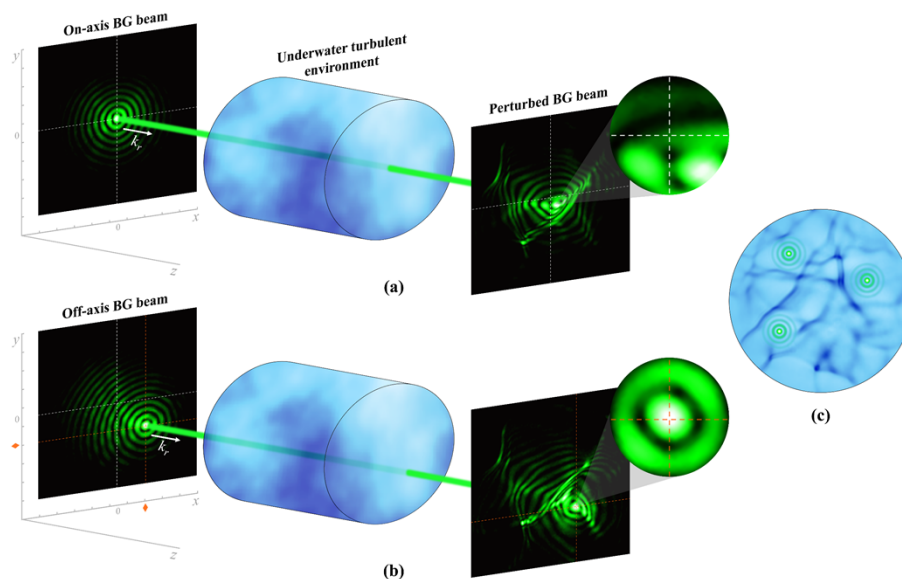


Fig. 1. (a) Propagation of an on-axis BG beam through an instance of turbulence. (b) Propagation of an off-axis BG beam through the same instance of turbulence. (c) Cross-section of the underwater turbulence depicting the complex spatial characteristics of a turbulent environment.

on-axis beam. The results herein show a marked reduction in beam wander and scintillation within the optimal paths when compared to a stationary BG beam, as well as the ability to transmit higher-order modes through the paths. Further, Fig. 1(c) shows a cross-section of the turbulent environment, providing a visualization of the complex spatial characteristics of the turbulence and indicating the possibility for multi-channel exploitation. Pertinent spatial and temporal characteristics of the unperturbed paths are analyzed and the ability to support simultaneous channels within the turbulence is demonstrated.

2. Off-axis Bessel-Gauss beams

As depicted in Fig. 1(c), an underwater turbulent environment creates an intricate spatial environment with a myriad of channels or paths in which a mode might propagate through with minimal perturbations. It is obvious from Fig. 1(c) that these unperturbed paths will not always align with some designated axis of propagation of an optical system, and the ability to shift a beam off-axis without altering the angle of propagation would be advantageous in fully identifying and exploiting these channels. This is demonstrated here through the use of an off-axis BG beam, which represents the shifting of the BG intensity distribution within the Gaussian envelope used to truncate the Bessel function [28]. This can be described as

$$E_{BG}(r, \phi) = \exp\left(\frac{-r^2}{w_G^2}\right) J_m(k_r R') \exp(-jm\Theta')^{\frac{m}{2}} \hat{y} \quad (1)$$

where r and ϕ are the polar coordinates of the position vector on the transverse plane, w_G represents the waist of the Gaussian envelope of the beam, J_m denotes the Bessel function of the first kind of order m , and k_r is the radial wave vector. The \hat{y} notation indicates the vertical polarization of the field and is consistent with experimentally generated fields described later. R' and Θ' represent the shifted radial and angular coordinates, respectively, defined as

$$R' = \sqrt{(r \cos \phi + \alpha)^2 + (r \sin \phi + \beta)^2} \quad (2)$$

$$\Theta' = \tan^{-1}\left(\frac{r \sin \phi + \beta}{r \cos \phi + \alpha}\right) \quad (3)$$

where α and β correspond to the shift of the beam's center in the x and y directions, respectively. The following section details the experimental setup that uses an input Gaussian beam to create a circular array of Gaussian beamlets, generating a non-diffracting, off-axis BG beam after a Fourier transform via a lens which then propagates through a volume of turbulence.

2.1. Beamlet generation of non-diffracting Bessel-Gauss beams

A modified HOBbit system, shown in Fig. 2, is used to generate a circular array of beamlets [29]. This system relies on two crucial components, an acousto-optic deflector (AOD), which generates a linear array of beamlets by deflecting the input beam, and a pair of log-polar optics, which perform a geometric transformation from Cartesian coordinates in the plane of the first log-polar optic to polar coordinates at the plane of the second log-polar optic, allowing the inputted linear array of beamlets to be mapped to a ring. The acoustic frequency of the signal supplied to the AOD is related to the first-order Bragg diffraction angle by $\theta = \frac{\lambda}{V} f$, where θ is the diffraction angle and λ is the optical wavelength. V and f are the acoustic velocity and frequency, respectively. This relationship between acoustic frequency and diffraction angle is leveraged to generate a simultaneous linear array of beamlets with varying tilts by supplying the AOD with a

signal, $S(t)$, that consists of many superimposed unique-frequency sinusoids, given by

$$S(t) = \sum_{n=0}^{N-1} A_n(t) \sin[2\pi f_n t + \varphi_n(t)] \quad (4)$$

where $N = 128$ is the number of beamlet locations. The parameters A_n , f_n and φ_n are the amplitude, frequency shift, and phase term of the n^{th} beamlet, respectively. The group of beamlets is Fourier transformed into a linear array by a single lens, after which each beamlet is mapped to a specific location around a perfect vortex (PV) envelope using a pair of log-polar diffractive optics. The field immediately after exiting the modified HOBBIT system can be represented as the superposition of these shifted Gaussian beamlets in the following form [29]:

$$E_{near}(\rho, \theta, t) = \exp\left(-\frac{t^2}{\tau_0^2}\right) \exp(-j2\pi f_c t) \sum_{n=0}^{N-1} D_n E_{n,near}(\rho, \theta) \exp(-j2\pi f_n t) \hat{y} \quad (5)$$

where ρ and θ are the polar coordinates of the position vector on the cross section of the beam. $D_n = A_n \exp(\varphi_n)$ is the complex amplitude of the n^{th} beamlet, f_c is the frequency of the input light and τ_0 represents the pulse width, indicating the use of a pulsed source for this system. The function $E_{n,near}$ represents the field of the n^{th} Gaussian beamlet on the ring, defined as

$$E_{n,near}(\rho, \theta) = \exp\left[-\frac{(\rho - \rho_0)^2}{\rho_0^2 w^2} - \frac{(\theta - \theta_n)^2}{w^2}\right] \quad (6)$$

where ρ_0 represents the ring radius, θ_n specifies the angular position on the ring, w refers to the $\frac{1}{2}$ angular width, and $\rho_0 w$ denotes the $\frac{1}{2}$ waist size of each Gaussian beamlet.

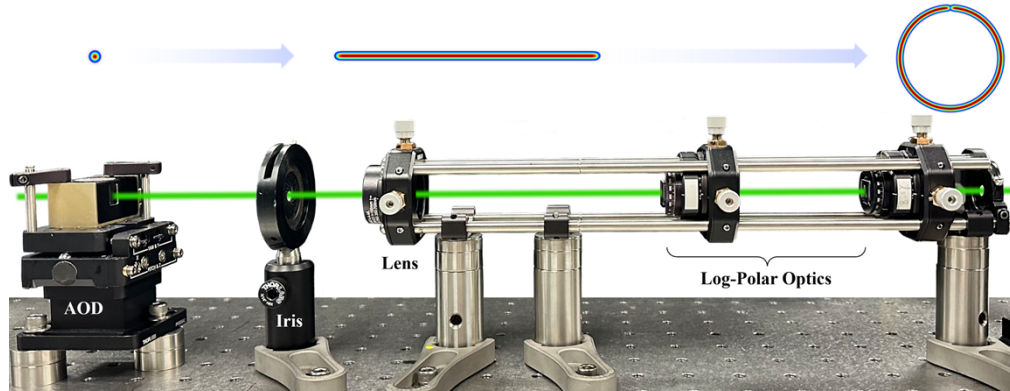


Fig. 2. Hardware of the modified HOBBIT system with overlays of the transverse beam profile along the propagation path.

To generate an off-axis BG beam from the circular array of beamlets, the complex amplitude distribution around the circular array of beamlets is first chosen as

$$D_n = \exp\left[i\zeta \left(\cos\left(2\pi \frac{n}{N} + \gamma\right) + \sin\left(2\pi \frac{n}{N} + \gamma\right)\right)\right] \quad (7)$$

The output field of the modified HOBBIT is then Fourier transformed at which point the chosen D_n in Eq. (7) corresponds to a shifting of the BG intensity distribution in the far field with ζ proportional to the radial shift from center and $\gamma \in [0, 2\pi]$ being the angle of the shift

with respect to the positive x-axis [30]. The far-field expression is described as a sum of larger titled Gaussian beamlets, derived as follows

$$E_{far}(r, \phi, t, z) = \exp \left[-\frac{t^2}{\tau_0^2} - j(2\pi f_c t) \right] \sum_{n=0}^{N-1} D_n(t) E_{n, far}(r, \phi) \exp(-j2\pi f_n t) \hat{y} \quad (8)$$

where r and ϕ are the polar coordinates of the position vector on the transverse plane in the far-field. The function $E_{n, far}$ represents the far-field of the n^{th} Gaussian beamlet, which is the Fourier transform of $E_{n, near}$, derived as

$$E_{n, far}(r, \phi, t) = \exp \left[-\frac{r^2}{w_G^2} - jr \frac{\rho_0 k}{F} \cos(\phi - \theta_n) \right] \quad (9)$$

where F is the focal length of the Fourier lens within the modified HOBBIT system, the parameter $k = 2\pi/\lambda$ is the wave vector of the beam, and the quantity w_G represents the waist of the Gaussian envelope of the beam in the far-field, and is given by

$$w_G = \frac{\lambda F}{\pi \rho_0 w} \quad (10)$$

Neglecting the frequency diversity for short pulses, $\tau_0 \ll (2\pi f_n)^{-1}$, we can approximate $f_n \cong f_0$, with f_0 being a constant value obtained by averaging the frequencies of the beamlets. By applying the Jacobi-Anger expansion, given by

$$\exp \left[-jr \frac{\rho_0 k}{F} \cos(\phi - \theta_n) \right] = \sum_{m=-\infty}^{\infty} j^m J_m \left(r \frac{\rho_0 k}{F} \right) e^{-jm(\phi - \theta_n)} \quad (11)$$

with J_m denoting the Bessel function of the first kind of order m , Eq. (8) can be rewritten as a discrete sum over Bessel functions of various orders as

$$E_{far}(r, \phi, t) = \exp \left[-\left(\frac{r^2}{w_G^2} + \frac{t^2}{\tau_0^2} \right) \right] \exp[-j2\pi(f_c + f_0)t] \sum_{m=-\infty}^{\infty} \tilde{D}_m J_m(k_r r) e^{-jm\phi} \hat{y} \quad (12)$$

where $k_r = (\rho_0 k)/F$ is the radial wave vector, and the set of coefficients \tilde{D}_m corresponds to the discrete Fourier transform of the series D_n , defined as

$$\tilde{D}_m = \sum_{n=0}^{N-1} D_n(t) e^{jm(\theta_n + \frac{\pi}{2})} \quad (13)$$

Well-localized by the Gaussian term and of a dominant angular mode, m , Eq. (12) is simplified into a single term representing an off-axis BG beam, and can be written as [28]

$$E_{far}(r, \phi, t) = \exp \left[-\left(\frac{r^2}{w_G^2} + \frac{t^2}{\tau_0^2} \right) \right] \exp[-j2\pi(f_c + f_0)t] J_m(k_r R') \exp(-jm\Theta')^{m/2} \hat{y} \quad (14)$$

Equation (14) shows that the far-field beam can be described as an off-axis BG beam with radial wave vector k_r . Since the primary factor influencing BG beam diffraction is the radial wave vector, and all combined beamlets share this value, the entire set of BG beams will exhibit uniform diffraction behavior as it propagates. Given this representation, the generated beams have a propagation distance over which they are considered non-diffracting. This is the region

where the beam maintains its shape before significant divergence occurs. It is governed by the Gaussian envelope that truncates the Bessel beam and can be represented by

$$\Delta z = \frac{w_G}{\alpha_c} \quad (15)$$

where $\alpha_c = \sin^{-1}((\lambda k_r)/2\pi)$ is the cone angle associated with the radial wave vector of the Bessel beam [31]. The experimental verification of this non-diffracting region for the generated beams is presented in our previous publication [29].

2.2. Experimental generation

Figure 3 illustrates the experimental setup for this work. A 517 nm pulsed laser with a pulse width of $\tau_0 = 239$ fs seeds the modified HOBBIT system [32]. The generation system is configured to produce $N = 128$ locations, where Gaussian beamlets of width, $\rho_0 w \approx 150$ μm , are evenly distributed around a PV envelope of radius $\rho_0 = 1.365$ mm. A lens with focal length $F_2 = 200$ mm Fourier transforms the circular array of beamlets, resulting in a non-diffracting BG mode as described previously. A 20x telescope resizes the beam which then propagates through the 3 m long UTE before being captured by a high-speed CCD. In the UTE, the central lobe of the BG beam is approximately 0.9 mm and the non-diffracting region of the beam is calculated to be $\Delta z = 16$ m, as per Eq. (15). Due to the log-polar wrapping, the ring width, $\rho_0 w$, varies slightly between the x and y dimensions. As a result, Δz was calculated separately in both the x and y directions, and the reported Δz represents an average that bounds the maximum distance for the non-diffracting behavior. It is noted that the entire propagation path between the telescope and the CCD is 7 m, well within this non-diffracting region.



Fig. 3. The modified HOBBIT system generates beams that are propagated through a turbulent underwater environment within the non-diffracting region before being captured with a CCD.

To experimentally generate the off-axis BG beams, the signal supplied to the AOD, $S(t)$, is altered such that the complex amplitude is as described in Eq. (7). This shifts the intensity distribution of the BG beams in the far field. Since the Fourier transform is performed by a single lens in the optical system, the x and y components of the physical distance of the shift (α and β) can be related to the signal parameters ζ and γ by

$$\alpha = \frac{F_2 \zeta}{k_r \rho_0} \cos(\gamma) \quad \text{and} \quad \beta = \frac{F_2 \zeta}{k_r \rho_0} \sin(\gamma) \quad (16)$$

Figures 4(a) and 4(b) are simulated images showing an on-axis and off-axis beam respectively, while Fig. 4(c) and 4(d) are experimental images generated using the optical system that depict an on-axis and off-axis BG beam respectively. For the off-axis BG beams (Fig. 4(b),(d)), $\alpha = 0.0043$ mm and $\beta = -0.0038$ mm. The experimental shift of the BG beam was measured to be within 1% of the theoretical values determined using Eq. (16).

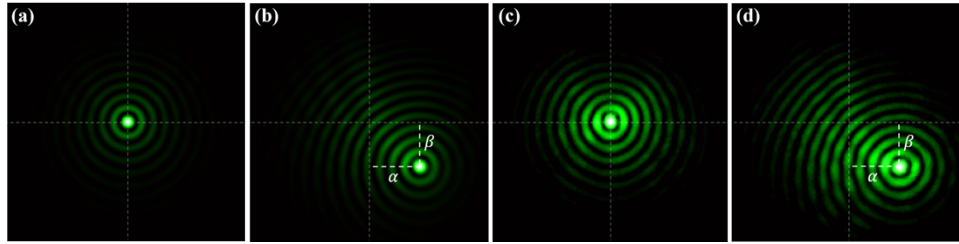


Fig. 4. (a) Simulated and (c) experimentally generated on-axis BG beam. (b) Simulated and (d) experimentally generated off-axis BG beam.

3. Rapid probing in underwater turbulence

This section first describes the parameterization of underwater turbulence in optics, followed by the implementation of the experimental scanning method with off-axis BG beams used to explore its impact on the beams' propagation.

3.1. Turbulent underwater environment and its effects on optical propagation

Underwater optical turbulence is induced by fluctuations of the refractive index in the underwater environment due to temperature variations. To quantify these fluctuations and subsequently characterize the turbulent environment, the index of refraction structure constant, C_n^2 , is commonly used. This parameter is an indicator of the strength of the turbulence and is crucial for understanding how it affects the propagation of light through the medium [33,34]. In this work, an underwater turbulence emulator (UTE) is used to create a stable and repeatable turbulent underwater environment. Depicted in Fig. 3, the UTE is a 3 m long, 100 mm diameter PVC tube that is fitted with optical windows on either end. It also features temperature components running along the length of the tube, creating a temperature gradient transverse to the direction of the beam propagation. The characterization process of the UTE is described in [35], and details the use of beam wander and temperature fluctuation measurements taken within the environment to calculate a refractive index structure constant of $C_n^2 \approx 10^{-10} \text{ m}^{-2/3}$.

When a beam propagates through a turbulent environment, the intensity of the beam fluctuates due to the refractive index variations in the environment. The variance of these intensity fluctuations is called the scintillation index, defined as [36]

$$\sigma_I^2 = \frac{\langle I^2 \rangle - \langle I \rangle^2}{\langle I \rangle^2} = \frac{\langle I^2 \rangle}{\langle I \rangle^2} - 1 \quad (17)$$

where I , $\langle I \rangle$, $\langle I^2 \rangle$ are the instantaneous intensity, average intensity, and the intensity variance over a designated region of the beam, respectively. The scintillation index is commonly used to designate the performance of a beam through a turbulent environment, with lower scintillation values indicating less perturbed transmission [22,37,38].

Another important parameter for characterizing the effects of turbulence on a beam is the beam wander [22,37,39]. A beam propagating through turbulent conditions will be deflected off of its axis, with the beam wander defining the variance of the displacement of a beam's maximum point of irradiance. This can be described as [36]

$$\langle r_c^2 \rangle = 2.42 C_n^2 z^3 w_0^{-\frac{1}{3}} \left(1 - \left(\frac{k_0^2 w_0^2}{1 + k_0^2 w_0^2} \right)^{\frac{1}{6}} \right) \quad (18)$$

where z is the propagation distance, w_0 is the beam width, respectively, and $k_0 = 2\pi/L_0$, where L_0 is the outer scale of the turbulence. For the described work, the maximum beam wander

displacement at three standard deviations (99.7%) is approximately 1.4 mm, providing an upper bound on the expected displacement of the beams propagated through the UTE.

3.2. Experimental implementation of a high-speed optical probe

With the ability to arbitrarily shift the center of the BG beam within the Gaussian envelope, a scanning sequence is designed to sample a designated probing space. In total, the scanning sequence consists of 95 steps, shifting the BG beam to 95 locations uniformly distributed over a circular area of 64 mm^2 using a concentric disk sampling method [40]. Both the azimuthal and radial spacing of the scan locations were set to 0.9 mm. Figure 5(a) depicts a map of the scanning locations, while Fig. 5(b) and Fig. 5(c) show experimental images of the beam at the first sequence step in ambient and turbulent conditions respectively. [Visualization 1](#) illustrates the beam scanning through an entire sequence in both ambient and turbulent conditions. It is important to note the fundamental difference with this probing method as compared to our previous work using beamlets on a perfect vortex ring, which corrected the tilt of an input beam to ensure optimal propagation through a turbulent volume [35,41]. The current method shifts the beam without introducing a tilt, ensuring that the propagation path of the beam remains transverse to the turbulent volume for all probing locations. In this work, the pulsed laser source is set to a repetition rate of 10 kHz, meaning a complete scan, consisting of 95 pulses, takes 9.5 ms to complete. It is noted that the turbulent environment changes on the order of hundreds of milliseconds and can be considered static for the duration of a scan, as is observed in [Visualization 1](#). The duration of the scanning sequence is constrained by the speed of the CCD used for imaging the beams and is not crucial to the functionality of the probing method. Fundamentally, the scanning speed of this system is limited by the time it takes for the acoustic signal to propagate across the input beam within the AOD, defined by $2w_0/V$ where V is the acoustic velocity of the TeO2 crystal in the AOD [35]. Under the current system parameters, this would allow the same scanning sequence described above to be completed in 125 μs .

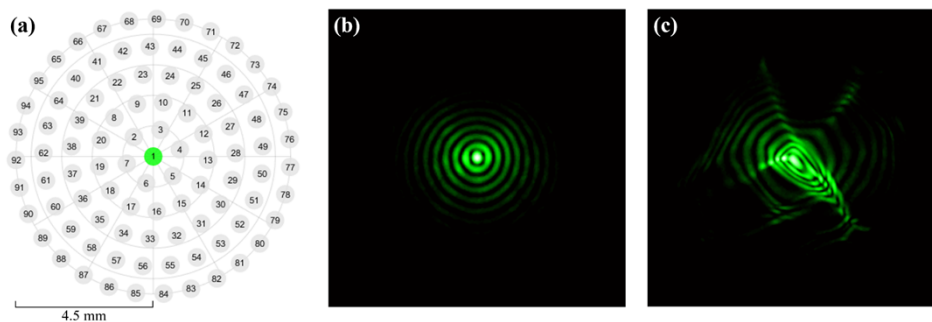


Fig. 5. (a) A map of the 95 locations of the BG beam in the scanning sequence. Experimental image of the beam at the first sequence step in (b) ambient and (c) turbulent conditions. (See [Visualization 1](#).)

4. Experimental results and analysis

In this work, a high-speed CCD was used to capture the beam profiles of the generated BG modes after propagation through the underwater turbulent environment. For a single scan as described in section 3.2, one beam profile is captured per scan position, resulting in 95 images collected per scan. Initially, data from 25 complete scans were taken in quiescent conditions (no turbulence induced in the UTE). The data was averaged over the 25 scans to account for experimental inconsistencies in the system, with the resulting dataset being used as a reference

and including one image per scan location. It is noted that in quiescent conditions, due to their non-diffracting nature, the beams are invariant over the entirety of the propagation path. Next, with turbulent conditions as described in section 3.1 present in the UTE, 200 consecutive scans were conducted at 25 ms intervals over 5 seconds, creating a dataset of 19,000 beam profiles.

4.1. Optimal transmission paths in underwater turbulence

To quantify the effects of the turbulent conditions on the transmitted modes, the spatial correlation of the intensity distributions between the unperturbed and perturbed beams was considered. This analysis accounts for any distortion and displacement that a beam may experience while propagating through the turbulence [42]. Given a scan through the turbulent underwater environment, the perturbed beam at each scan position was compared to a beam in the corresponding position under quiescent conditions. The unshifted spatial correlation between the beam profiles was calculated over a 3 mm circular region of interest (ROI) of the images centered on the central lobe of the relatively unperturbed BG beam. To ensure that any breakup or deflection experienced by the beam due to the turbulence would be reflected in the analysis, the size of the ROI was chosen to be consistent with the maximum beam wander displacement expected in the UTE. The correlation is given by

$$C = \frac{\sum_x \sum_y I_1(x, y) \cdot I_2(x, y)}{\sqrt{\sum_x \sum_y I_1^2(x, y)} \cdot \sqrt{\sum_x \sum_y I_2^2(x, y)}} \quad (19)$$

where $I_1(x, y)$ and $I_2(x, y)$ are the intensity values of the reference beam and perturbed beam, respectively. Figure 6 depicts two examples of the effects of turbulence on the propagated modes, with Fig. 6(a), (b) depicting both (a) a reference beam and (b) a perturbed beam at the same scanning position, the white circle indicating the ROI, and the inset image providing an enlarged view of this region. In this instance, it is observed that the beam is only minorly distorted by the turbulence, maintaining a high correlation value with the corresponding reference beam. Comparatively, Fig. 6(c), (d) illustrates an instance when the (d) perturbed beam is heavily distorted and shifted compared to the (c) reference beam, resulting in a low correlation value. By calculating the correlation value for each image in the dataset, optimal transmission paths are identified within the turbulent volume.

Bounding the effects of the turbulence on the transmitted beams, the minimum correlation value per scan, C_{min} , and the highest correlation value per scan, C_{opt} , were determined for each of the 200 scans. In Fig. 6(e), C_{opt} and C_{min} are plotted over the 5 second data acquisition period as the solid green line and dotted red line, respectively. Each value of C_{opt} corresponds to a scan location where the beam propagated through that instantaneous turbulence realization least perturbed, representing the optimal transmission path identified by this probing method. Since many optical systems reflected in current literature utilize a stationary, on-axis BG beam, it is necessary to compare the results of a stationary case with C_{opt} . As indicated in Fig. 5, an on-axis BG beam is the first position in each scan, and the correlation value for this position per instance of turbulence, C_1 , is represented by the blue dashed line in Fig. 6(e). It is observed that the stationary BG beam experiences large fluctuations in correlation due to the effects of the dynamic turbulence, with an average correlation value of 0.66 and standard deviation of 0.11. Comparatively, C_{opt} averaged a correlation value of 0.90 with a standard deviation of 0.03, indicating the effectiveness of the probing method to reduce the effects of turbulence on an optical beam by identifying minimally perturbed transmission paths through the turbulent volume.

To further demonstrate the functionality of the optical probing system, datasets were collected using higher-order BG modes to scan the turbulent volume. The data collection and analysis methods described above were replicated to generate data for OAM values, $M = (-4, -2, +2, \text{ and } +4)$. Figure 7(a)-(d) depicts instances of the higher-order beams scanning in (a), (c) quiescent and (b), (d) turbulent conditions with (a), (b) $M = -2$ and (c), (d) $M = +4$. Figure 7(e) compares

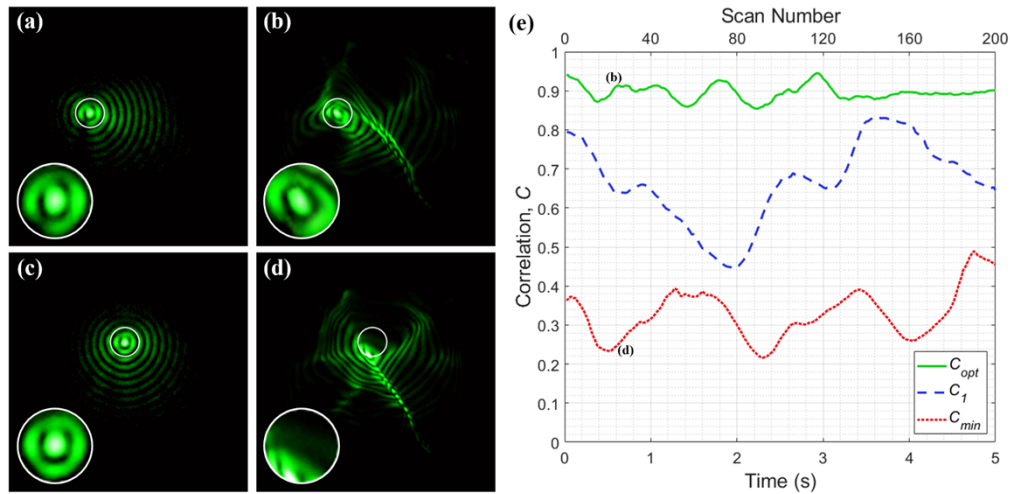


Fig. 6. (a) Reference beam and (b) perturbed beam at the same scan position showing an example of minimal distortion and high correlation within the central region of the beam. (c) Reference beam and (d) perturbed beam at the same scan position showing an example of noticeable distortion and low correlation within the central region of the beam. (e) Graph displays the maximum correlation per scan, C_{opt} , the minimum correlation per scan, C_{min} , and the correlation of an unshifted BG beam, C_1 , across the 5 second data acquisition period.

the system performance for each of these modes by plotting C_{opt} in time for each M value as well as C_{opt} of the initial dataset with $M = 0$. It is noted that a respective dataset is taken during a unique 5 s period of turbulence for each OAM value, and the scanning position at which C_{opt} was obtained varied due to the dynamic spatial distributions of the turbulence. It is observed that as $|M|$ increases, the average C_{opt} slightly decreases. This is likely due to the increase in spatial footprint as the mode number increases, making the larger beams more susceptible to the effects of the turbulence. Regardless, the probing system identifies high-fidelity transmission paths for all values of M , indicating the ability to transmit high-order modes through the underwater turbulence relatively unperturbed. These results demonstrate the proclivity of these channels to support high bandwidth optical communication links through spatial division multiplexing [43].

While the previous results indicate the described probing system's ability to identify unperturbed transmission paths within a turbulent volume where the effects of beam wander are minimized, it is necessary to also consider the scintillation of the beams traveling along these paths. To further compare the performance of the beams traveling along these identified channels to a stationary, on-axis BG beam, the scintillation was measured for both cases at OAM values $M = (-4, -2, 0, +2, \text{ and } +4)$. For all scintillation measurements, the point of maximum power in quiescent conditions was used, located in the central lobe of the 0th-order BG beam and in the annulus of the higher-order vortex beams. In Fig. 8, the red circles depict the scintillation index over a 5 second period for a stationary, on-axis beam, C_1 , for each respective OAM value. Comparatively, the green circles indicate the scintillation index over the same 5 second period given the optimal transmission path identified per scan, C_{opt} , for each respective OAM value. For all OAM values, it is observed that the scintillation index of the beam traveling through the optimal paths identified by the system is drastically reduced compared to that of the stationary, on-axis beam. The scintillation values for C_1 and C_{opt} are reported in Table 1, along with the percent reduction in scintillation between the two cases. The reduction in scintillation is greatest for the case of the 0th-order BG beam, being reduced by over 91% from C_1 to C_{opt} , while the reductions in the higher-order modes range from 64% to 84%. This further indicates the efficacy

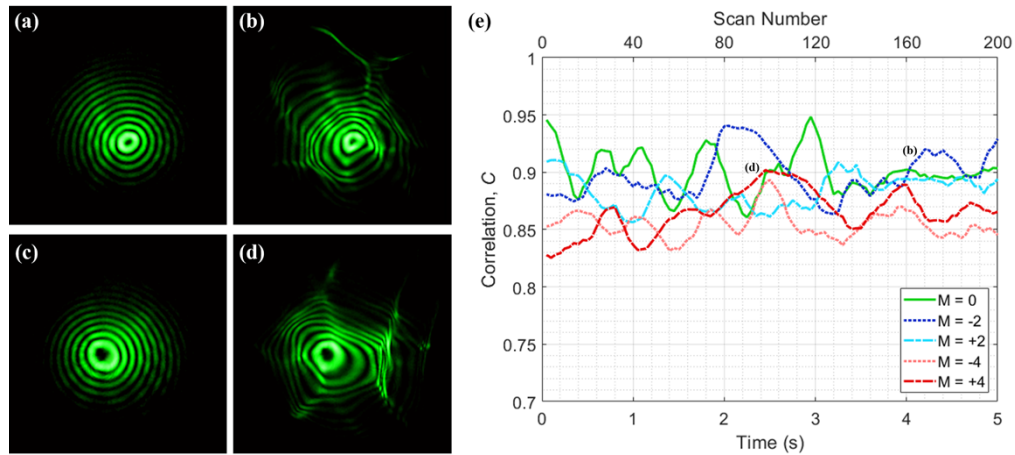


Fig. 7. With $M = -2$, (a) a reference beam and (b) perturbed beam are shown at the same scan position. With $M = +4$, (c) a reference beam and (d) perturbed beam are shown at the same scan position. (e) The maximum correlation values per scan, C_{opt} , for OAM values, $M = (-4, -2, 0, +2, +4)$. 200 scans were conducted over a unique 5 s time period for each respective OAM value.

of the probing system in determining transmission paths that are relatively unperturbed by the turbulent effects, resulting in lower scintillation.

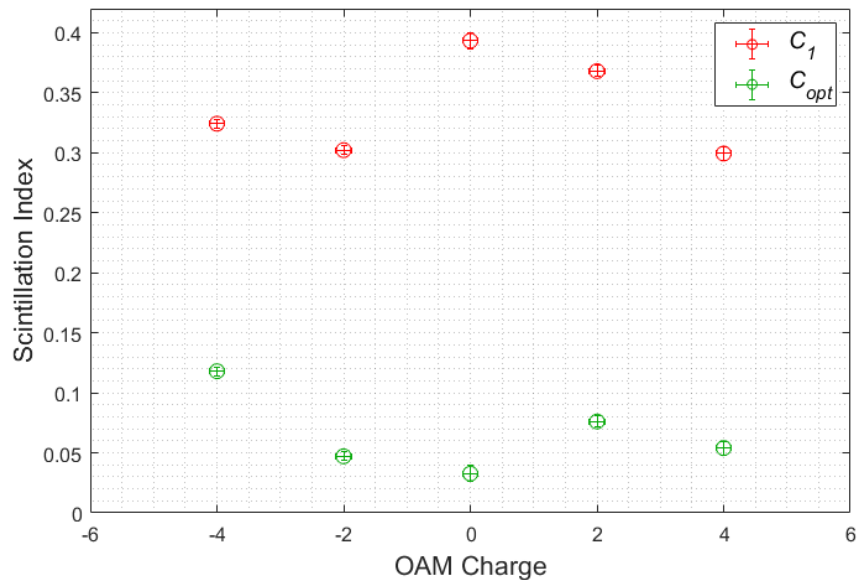


Fig. 8. Scintillation index of a stationary, on-axis beam, C_1 , and the optimal transmission path identified per scan, C_{opt} , for various OAM values, $M = (-4, -2, 0, +2, +4)$.

4.2. Spatiotemporal characteristics of the optimal transmission paths

By taking 200 scans at 25 ms intervals over a total time of 5 seconds, with each scan consisting of 95 unique positions covering a circular area, both the temporal and spatial characteristics of the

Table 1. Scintillation index measurements for stationary beam and optimal beam

OAM Charge	Scintillation Index C_1	Scintillation Index C_{opt}	Reduction in SI (%)
-4	0.3242	0.1180	63.6
-2	0.3022	0.0471	84.4
0	0.3933	0.0327	91.7
+2	0.3680	0.0761	79.3
+4	0.3015	0.0542	82.0

propagation paths through the underwater turbulence can be studied. Figure 9(a) is a visualization of the collected data in the 5 second period scanning with the 0th-order BG beam, with each row corresponding to a single scan position and each column representing a complete scan at an instance in time. The color of each pixel in Fig. 9(a) indicates the correlation value, C , for the corresponding scan position and instance in time, with yellow indicating higher C values and blue indicating lower C values. To further characterize the optimal transmission paths within the turbulent volume, realizations with C values greater than 0.8 were considered. These instances of relatively unperturbed transmission are displayed as the opaque regions in the dataset in Fig. 9(b) and comprise 11.6% of the realizations collected, indicating the prevalence of these paths in the underwater turbulent environment. The persistence of these high-fidelity transmission paths was analyzed by determining the individual lengths of the highlighted regions along each row of Fig. 9(b). Figure 9(c) is a histogram of the persistence values, showing the distribution of the persistences for the identified instances. The persistences of these transmission paths range from 25 ms to 1.575 s, with a median and mean value of 350 ms and 444 ms, respectively. The temporal characteristics of these channels are indicative of the underwater turbulence, and the results match previous work within the same turbulent environment that describes the turbulence changing on the order of hundreds of ms [35].

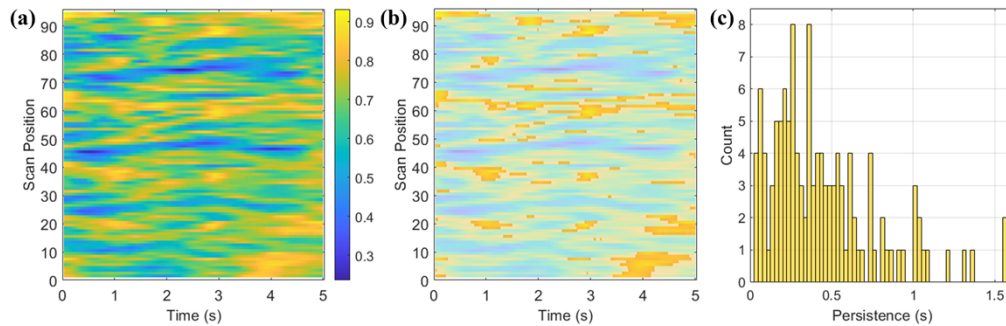


Fig. 9. (a) Correlation values (color) for each scan position over 200 consecutive scans taken in 5 s. (b) Opaque regions indicate high-fidelity transmission paths ($C > 0.8$) within the dataset. (c) Histogram showing the distribution of persistences of the high-fidelity transmission paths.

While the temporal characteristics of the unperturbed transmission paths were determined through a row-by-row analysis of the data presented in Fig. 9(a), (b), the spatial distribution of these high-fidelity channels can be determined through a column-by-column analysis of the same data. In Fig. 9(a),(b), each column represents a single scan through all 95 positions, completed during an instantaneous realization of the turbulent environment. Figure 10(a) displays the data associated with a single scan as a spatial map of all 95 scan positions, with the color of each marker indicating the correlation value of that scan position for the given realization

of the turbulence. In Fig. 10(a), as in Fig. 9(b), the opaque markers indicate the relatively unperturbed transmission paths ($C > 0.8$). For the scan depicted in Fig. 10(a), it is observed that the high-fidelity transmission paths create three distinct regions within the scanned area, indicating the size and density of these channels for this realization of turbulence. Over the 200 scans taken within the 5 second period, an average of 11 scan positions demonstrated minimal perturbations per scan, creating an average of 3 spatially separated regions per scan. This result indicates the existence of multiple channels that can be exploited simultaneously [44]. To further demonstrate, Fig. 10(b) depicts an incoherent superposition using two of the beam profiles from different scan positions within the scan shown in Fig. 10(a). Both of the scan positions shown in Fig. 10(b) propagated through the turbulence relatively unperturbed and are outlined in black in Fig. 10(a). The correlation between the respective intensity profiles of the two modes displayed in Fig. 10(b) is found to be 0.22 using Eq. (19). In this example, the low correlation value indicates relatively little spatial overlap between the two unperturbed modes after propagation through the turbulence, illustrating the propensity to exploit simultaneous channels with minimal interference within a dynamic, turbulent underwater environment.

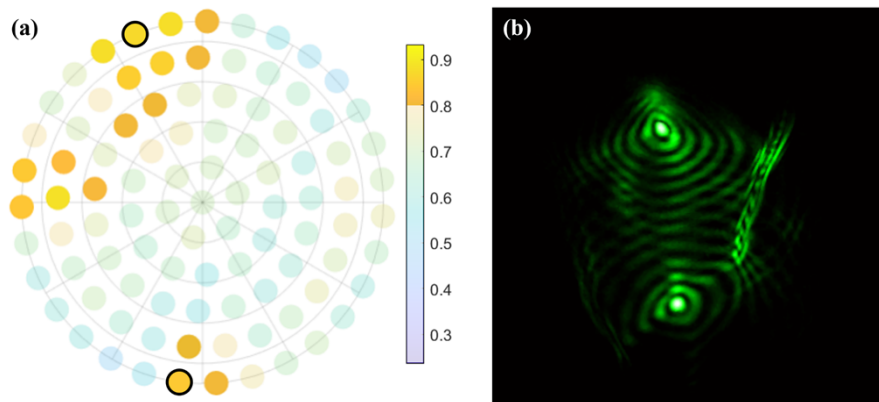


Fig. 10. (a) Correlation values (color) of each position for a single scan completed during an instantaneous realization of turbulence. (b) A superposition of intensity profiles indicates the existence of two unperturbed transmission paths existing simultaneously within the turbulence.

5. Conclusion

The propagation of light through turbulent media remains a major challenge for the realization of optical systems in underwater environments. Towards this goal, there have been numerous works demonstrating unperturbed transmission through static turbulent paths, outlining a fundamental approach to optimized propagation through disordered media [24–26]. Extending this idea to a real-world dynamic environment, this work describes the experimental generation and manipulation of off-axis BG modes to achieve unperturbed propagation through an underwater turbulence environment. A modified HOBBIT system rapidly scans the non-diffracting modes within a probing volume, allowing transmission channels that suffer minimal effects from the turbulence to be identified. The results demonstrate that the beams propagated through the minimally perturbed channels experience largely reduced effects of the turbulence, including over a 91% reduction in scintillation index, when compared to an on-axis, stationary BG beam. Additionally, higher-order off-axis BG modes were successfully transmitted through the optimal channels, demonstrating the possibility for these paths to support high data rate optical communication links through multiplexing and demultiplexing [43]. The prevalence of

these unperturbed transmission paths is reported as 11.6% of all probed realizations with an average channel persistence of 444 ms, and the propensity for simultaneous channel exploitation is demonstrated. The experimental realization of unperturbed propagation through a complex turbulent environment alongside the analysis and discussion of certain channel characteristics is an important step towards the realization of robust optical systems in real-world environments. Expanding further upon this work, preliminary results demonstrate the feasibility of application-tailored modes for specific purposes through a turbulent volume, indicating further optimizations of optical systems including sensing and imaging and optical communications in real-world environments.

Funding. Office of Naval Research (N00014-20-1-2558).

Disclosures. The authors declare no conflicts of interest.

Data availability. Data underlying the results presented in this work are not publicly available at this time but may be obtained from the authors upon reasonable request.

References

1. G. Schirripa Spagnolo, L. Cozzella, and F. Leccese, "Underwater Optical Wireless Communications: Overview," *Sensors* **20**(8), 2261–2274 (2020).
2. M. Yousefi, F. Dabbagh Kashani, A. Aghajani, *et al.*, "Experimental study of the effects of thermally induced optical turbulence on underwater wireless optical communication link parameters," *J. Opt.* **22**(2), 025702 (2020).
3. H. M. Oubei, E. Zedini, R. T. ElAfandy, *et al.*, "Simple statistical channel model for weak temperature-induced turbulence in underwater wireless optical communication systems," *Opt. Lett.* **42**(13), 2455–2458 (2017).
4. E. Zedini, H. M. Oubei, A. Kammoun, *et al.*, "Unified Statistical Channel Model for Turbulence-Induced Fading in Underwater Wireless Optical Communication Systems," *IEEE Trans. Commun.* **67**(4), 2893–2907 (2019).
5. Z. Vali, A. Gholami, Z. Ghassemlooy, *et al.*, "Experimental study of the turbulence effect on underwater optical wireless communications," *Appl. Opt.* **57**(28), 8314–8319 (2018).
6. X. Yi, Z. Li, and Z. Liu, "Underwater optical communication performance for laser beam propagation through weak oceanic turbulence," *Appl. Opt.* **54**(6), 1273–1278 (2015).
7. Y. Baykal, "Signal-to-noise ratio reduction due to oceanic turbulence in oceanic wireless optical communication links," *Opt. Commun.* **427**, 44–47 (2018).
8. H. Gerçekcioğlu, "Bit error rate of focused Gaussian beams in weak oceanic turbulence," *J. Opt. Soc. Am. A* **31**(9), 1963–1968 (2014).
9. M. C. Gökçe, Y. Baykal, and Y. Ata, "Effects of adaptive optics on bit error rate of M-ary PPM oceanic optical wireless communication systems with aperture averaging in strong turbulence," *Laser Phys.* **31**(11), 115204 (2021).
10. L. Zhu, H. Yao, H. Chang, *et al.*, "Adaptive Optics for Orbital Angular Momentum-Based Internet of Underwater Things Applications," *IEEE Internet Things J.* **9**(23), 24281–24299 (2022).
11. M. V. Jamali, P. Nabavi, and J. A. Salehi, "MIMO Underwater Visible Light Communications: Comprehensive Channel Study, Performance Analysis, and Multiple-Symbol Detection," *IEEE Trans. Veh. Technol.* **67**(9), 8223–8237 (2018).
12. K. P. Peppas, A. C. Boucouvalas, and Z. Ghassemlooy, "Performance of underwater optical wireless communication with multi-pulse pulse-position modulation receivers and spatial diversity," *IET Optoelectron.* **11**(5), 180–185 (2017).
13. Y. Fu, Q. Duan, C. Huang, *et al.*, "Average BER performance of rectangular QAM-UWOC over strong oceanic turbulence channels with pointing error," *Opt. Commun.* **476**, 126362 (2020).
14. W. Liu, Z. Xu, and L. Yang, "SIMO detection schemes for underwater optical wireless communication under turbulence," *Photonics Res.* **3**(3), 48–53 (2015).
15. A. Forbes, M. D. Oliveira, and M. R. Dennis, "Structured light," *Nat. Photonics* **15**(4), 253–262 (2021).
16. L. Allen, M. W. Beijersbergen, R. J. C. Spreeuw, *et al.*, "Orbital angular momentum of light and the transformation of Laguerre-Gaussian laser modes," *Phys. Rev. A* **45**(11), 8185–8189 (1992).
17. A. M. Yao and M. J. Padgett, "Orbital angular momentum: origins, behavior and applications," *Adv. Opt. Photonics* **3**(2), 161–204 (2011).
18. S. M. Lloyd, M. Babiker, G. Thirunavukkarasu, *et al.*, "Electron vortices: Beams with orbital angular momentum," *Rev. Mod. Phys.* **89**(3), 035004 (2017).
19. H. E. Hernández-Figueroa, E. Recami, and M. Zamboni-Rached, eds., *Non-Diffracting Waves* (Wiley-VCH Verlag GmbH & Co. KGaA, 2014), Chap. 1.
20. J. Durnin, "Exact solutions for nondiffracting beams I The scalar theory," *J. Opt. Soc. Am. A* **4**(4), 651–654 (1987).
21. F. Gori, G. Guattari, and C. Padovani, "Bessel-Gauss beams," *Opt. Commun.* **64**(6), 491–495 (1987).
22. S. R. Lekshmi and C. S. Narayanamurthy, "The resilience of zero order Bessel-Gaussian Beams to the impact of dynamic Kolmogorov type of turbulence," *Opt. Commun.* **532**, 129243 (2023).
23. Y. Wang, P. Zhang, X. Wang, *et al.*, "Performance analysis on free space underwater data transmission using Bessel-Gaussian beams in a simulated ocean channel with various effects," *Opt. Commun.* **473**, 125969 (2020).

24. A. Klug, C. Peters, and A. Forbes, "Robust structured light in atmospheric turbulence," *Adv. Photonics* **5**(01), 016006 (2023).
25. V. N. Shatokhin, D. Bachmann, G. Sorelli, *et al.*, "Spatial eigenmodes of light in atmospheric turbulence," in *Environmental Effects on Light Propagation and Adaptive Systems III*, K. Stein and S. Gladysz, eds. (SPIE, 2020), pp. 12–20.
26. C. Peters, I. Nape, and A. Forbes, "A spatial mode description of robust states of structured light through complex media," *arXiv* (2025).
27. W. Li, K. S. Morgan, Y. Li, *et al.*, "Rapidly tunable orbital angular momentum (OAM) system for higher order Bessel beams integrated in time (HOBBIT)," *Opt. Express* **27**(4), 3920–3934 (2019).
28. S. K. Singh, K. Kinashi, N. Tsutsumi, *et al.*, "Tricomi–Gauss beam and its propagation characteristics," *Opt. Quant. Electron.* **55**(4), 352 (2023).
29. T. Cramer, J. K. Miller, M. Reid, *et al.*, "Higher order Bessel beams integrated in time (HOBBIT) with engineered light frequencies (ELFs)," *Opt. Express* **32**(20), 34966–34975 (2024).
30. P. Khorin and A. Ustinov, "The formation of diffraction-free beams with a given distribution based on the Whittaker integral," in *International Conference on Information Technology and Nanotechnology* (IEEE, 2020), pp. 1–5.
31. G. Gbur, *Singular Optics*, Series in Optics and Optoelectronics (CRC Press, Taylor & Francis Group, 2017), Chap. 12.
32. J. K. Miller, D. Tsvetkov, P. Terekhov, *et al.*, "Spatio-temporal controlled filamentation using higher order Bessel-Gaussian beams integrated in time," *Opt. Express* **29**(13), 19362–19372 (2021).
33. G. Nootz, E. Jarosz, F. R. Dalgleish, *et al.*, "Quantification of optical turbulence in the ocean and its effects on beam propagation," *Appl. Opt.* **55**(31), 8813–8820 (2016).
34. G. Nootz, S. Matt, A. Kanaev, *et al.*, "Experimental and numerical study of underwater beam propagation in a Rayleigh–Bénard turbulence tank," *Appl. Opt.* **56**(22), 6065–6072 (2017).
35. J. P. Wiley, E. Robertson, N. A. Ferlic, *et al.*, "High data-rate communication link supported through the exploitation of optical channels in a characterized turbulent underwater environment," *Opt. Express* **31**(20), 31839–31852 (2023).
36. L. C. Andrews and R. L. Phillips, *Laser Beam Propagation Through Random Media*, Second (International Society of Optical Engineering, 2005), Chap. 6.
37. N. A. Ferlic, S. Avramov-Zamurovic, O. O'Malley, *et al.*, "Randomness of optical turbulence generated by Rayleigh–Bénard convection using intensity statistics," *J. Opt. Soc. Am. A* **41**(6), B85–B94 (2024).
38. J. Wiedemann, C. Nelson, and S. Avramov-Zamurovic, "Scintillation of laser beams carrying orbital angular momentum propagating in a near-maritime environment," *Opt. Commun.* **458**, 124836 (2020).
39. H. Kaushal, V. Kumar, A. Dutta, *et al.*, "Experimental Study on Beam Wander Under Varying Atmospheric Turbulence Conditions," *IEEE Photonics Technol. Lett.* **23**(22), 1691–1693 (2011).
40. P. Shirley and K. Chiu, "A Low Distortion Map Between Disk and Square," *Journal of Graphics Tools* **2**(3), 45–52 (1997).
41. M. Lemon, E. Robertson, J. Free, *et al.*, "Sensing and coupling of optical channels in dynamic atmospheric turbulence using OAM beamlets for improved power and data transmission," *Opt. Express* **30**(26), 47598–47611 (2022).
42. L. Devaud, B. Rauer, S. Mauras, *et al.*, "Correlating light fields through disordered media across multiple degrees of freedom," *Phys. Rev. Research* **6**(3), 033265 (2024).
43. Y. Ren, L. Li, Z. Wang, *et al.*, "Orbital Angular Momentum-based Space Division Multiplexing for High-capacity Underwater Optical Communications," *Sci. Rep.* **6**(1), 33306 (2016).
44. J. P. Wiley, E. Robertson, J. K. Miller, *et al.*, "Simultaneous Realization of Multiple Optical Channels in a Turbulent Underwater Environment," in *Optica Imaging Congress (3D, COSI, DH, FLatOptics, IS, pcAOP)* (Optica Publishing Group, 2023), PW5F.1.